

Computational Study of Particle Separation Based on Inertial Effects in Rectangular Serpentine Channels with Different Aspect Ratios

Alžbeta Bugáňová¹ ^a and Ivan Cimrák^{1,2} ^b

¹*Cell-in-fluid Biomedical Modelling & Computations Group, Faculty of Management Science and Informatics, University of Žilina, Slovakia*

²*Research Centre, University of Žilina, Slovakia, Slovak Republic*

Keywords: Inertial Microfluidics, Rectangular Cross-Section, Particle Separation, Focusing Length.

Abstract: Inertial effects in straight and curved microfluidic channels have great potential for separation of particles of different sizes. The geometry of the channels influences the separation. In this work we consider a serpentine channel with rectangular cross section of different sizes to explore the influence of aspect ratio on focusing performance and particle separation possibilities. Particle trajectories of different sizes are studied by means of a computational simulations. We show that low-aspect ratio offers more possibilities for separation in terms of particle sizes as well as in terms of higher throughput.

1 INTRODUCTION

The inertial migration of particles in a flow through a cylindrical tube was first observed by (Segré and Silberberg, 1961). In their experiments, spherical particles migrated to an annulus located about 0.6 times of tube radius between centerline and pipe wall. Subsequently, many research studies were focused to understand the underlying physics of this phenomenon through experimental studies, theoretical analyses and numerical simulations (McLaughlin, 1993; Chun and Ladd, 2006; Hood et al., 2015) and the references therein.

After big leap in microfluidics in last decades, where the size of patterned micro-channel is comparable to that of the suspended particles (so that inertial migration can be more obvious within a short channel length), inertial effects have found their use in practical applications in medicine and biomedicine e.g. recovery of rare cells from blood (Tanaka et al., 2012), separation of particles by deformability for instance diseased red blood cells from healthy ones or search for sepsis markers (Gossett et al., 2012).

Inertial microfluidics provide precise manipulation with immersed particles or cells, simple structure and high throughput. In contrast to active microfluidic manipulation technologies (Cetin and Li, 2011;

Forbes and Forry, 2012; Li et al., 2013) where external force fields (electric, magnetic, acoustic) are supplied to control the motion of target particles or cells, inertial microfluidics is a passive manipulation technology, and it employs intrinsic hydrodynamic force for manipulation. Therefore, the operation of inertial microfluidics is very simple and robust, and the cost of inertial microfluidic device is low.

Computational models provide effective way for prototyping the correct geometries of the channels. (Rasooli and Çetin, 2018) developed a Lagrangian model using COMSOL Multiphysics to solve the continuous phase and simulate particle trajectories in a spiral microchannel. (Jiang et al., 2016) explored the particle focusing mechanisms of a symmetric serpentine microchannel using model based on a lattice Boltzmann method. (Ying and Lina, 2020) studied special zig-zag shape of serpentine channel concluding several advantages of this type of channel compared to squared or curved serpentine. Their results indicate that the zigzag channel has the best focusing effect at a high Reynolds number and that the serpentine channel is second in terms of performance.

Contents of This Work

In this work we focus on studying how different aspect ratio of the channel cross section affects the eventual focusing positions of particles with two different sizes. In (Ying and Lina, 2020) the authors consid-

^a  <https://orcid.org/0000-0001-6772-2970>

^b  <https://orcid.org/0000-0002-0389-7891>

ered the cross section with dimensions $80 \times 40 \mu\text{m}$. We added two more cases to see whether more square-like cross section or a cross section with lower aspect ratio will affect the stable positions. Therefore we picked rectangular cross sections $60 \times 52 \mu\text{m}$ and $100 \times 32 \mu\text{m}$, see Figure 7. All three cases have similar area of around $3100 \mu\text{m}^2$. This ensures that with the same volumetric flow we get similar maximal velocities in the channels.

In Section 2 we briefly provide theoretical aspects of inertial focusing. In Section 3 we describe the physical model and its numerical implementation together with several technical details about the experimental setup. In Section 4 we provide computational results and in the last section we discuss the results.

2 PRINCIPLES OF INERTIAL FOCUSING

Particle focusing in straight channels about 60% away from the tube centerline is caused by a balance of inertial shear gradient lift forces pushing the particles towards the wall and a wall repulsion forces caused by an increased pressure between the particles and the wall (Matas et al., 2009). Altering the channel cross section or curving the channel into serpentine or spiral geometries changes the number and location of lateral equilibrium positions and can accelerate lateral focusing of particles (Martel and Toner, 2014). The forces responsible for such behaviour are three-

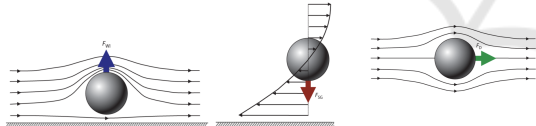


Figure 1: Competing inertial forces. Reprinted from (Martel and Toner, 2014) with permissions.

fold: the wall interaction lift forces, the shear gradient lift forces and the secondary-flow induced Dean drag forces, see Figure 1. As the streamlines are diverted toward the side of the particle away from the wall, the fluid accelerates, causing low pressure on the top and higher pressure on the wall side of the particle, which generates the wall interaction force, Figure 1 on the left. The formula giving the magnitude of the wall induced force is

$$F_{LW} = C_W \rho U_{max}^2 a^6 / D_h^4, \quad (1)$$

where C_W is a lift coefficient dependent on particle position and on Reynolds number (Di Carlo et al., 2009), ρ is the fluid density, U_{max} is the maximal fluid velocity, a is the particle diameter, and D_h is the hydraulic diameter of the channel.

A typical microfluidic velocity profile is parabolic and, thus, curved. A particle at a position in such a flow will experience velocities of different magnitudes on either side. The fluid flow around the particle must compensate for this difference and induces a force on the particle directed toward the side of the particle with a higher relative velocity (normally toward the walls of a microfluidic channel or areas of increasing shear), Figure 1 in the middle. This shear induced lift force has magnitude

$$F_{LS} = C_S \rho U_{max}^2 a^3 / D_h, \quad (2)$$

here C_S is a shear coefficient dependent on particle position and on Reynolds number (Di Carlo et al., 2009).

In curved channels, the centrifugal force generates a secondary flow that is perpendicular to the main flow direction. Normally, this flow is two orders magnitude weaker than the main flow, however it is sufficient to create the drag around the particles causing transversal motion across the cross section, Figure 1 on the right. The formula for the evaluation of Dean force takes the form

$$F_D = 3\pi\mu a U_D, \quad (3)$$

where averaged Dean velocity can be approximated by (Ookawara et al., 2004)

$$U_D = 1.8 \cdot 10^{-4} De^{1.63}. \quad (4)$$

Here, De denotes Dean number given by

$$De = Re \sqrt{\frac{D_h}{2R_c}} = \frac{\rho U_{max} D_h}{\mu} \sqrt{\frac{D_h}{2R_c}}, \quad (5)$$

Re being the Reynolds number and R_c the curvature radius of the channel.

The interplay between the wall and shear induced forces and the Dean force determines the cross sectional trajectory of a particle. There are however numerous assumptions for the validity of provided formulas, such as straight channels for lift forces and curved channels for Dean forces, which are not possible to be met simultaneously. Also, position dependent coefficients C_S, C_W cause the evaluation of the forces difficult. Therefore the actual simulations of the channel flow with immersed particles are extremely useful for studying the stabilized positions after focusing.

Inertial microfluidics can be categorized according to the shape of the channels: straight, spiral, serpentine channels and so called contraction-expansion array (CEA). Common feature of all these channels is the branching the main channel at the end into several output channels collecting particles of different sizes or a particle-free fluid, see Figure 2.

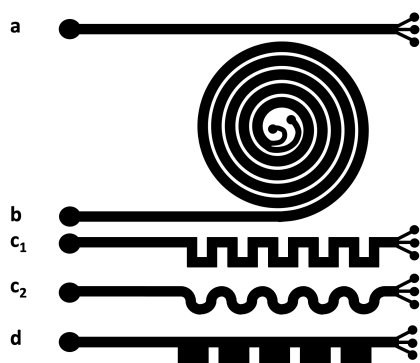


Figure 2: Typical shapes of channels used in inertial microfluidics (a) straight (b) spiral (c₁) square serpentine (c₂) curved serpentine and (d) CEA channels. Large black circles represent inflow of the suspension and several smaller circles represent outflow with separated particles.

Although we focus on serpentine channels, we briefly sum up the results concerning stabilized positions of particles in straight channels with rectangular cross-section. We need this, because as can be seen in Figure 2 (c₁) and in close detail in Figure 3, the first part of the channel is often straight and the particles tend to focus before entering the serpentine part. This must be taken into account when seeding the particles or cells at the inflow of the serpentine channel in the simulation.

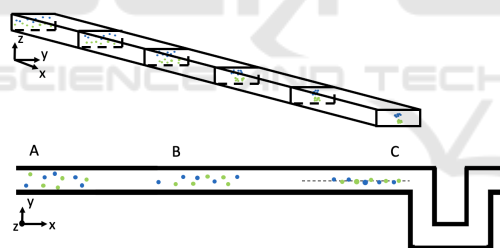


Figure 3: Focusing of particles before entering the serpentine part of the channel. Blue particles are in the upper part and the green particles in the lower part of the channel. Sector A - particles are distributed across the whole cross section coming from the inlet. Sector B - particles are being focused. Sector C - before entering the serpentine, the particles are focused in two (or four) positions.

The thorough numerical analysis confirmed by comparison with experimental results has been provided by (Mashhadian and Shamloo, 2019). The authors show a detailed analysis of stabilized positions of particles various sizes in straight rectangular channels depending on the channel Reynolds number and the channel aspect ratio. They show (see Figure 4) different stabilized positions in a rectangular cross section: center of short walls (red), center of long walls (yellow) and two other positions near long wall (green). Therefore we are able to derive stable posi-

tions at the entrance of our serpentine channels. This is done later in Section 3.4.

We must emphasize that straight channels are not suitable for separating particles of different sizes due to the similarity of focused positions for particles of different sizes.

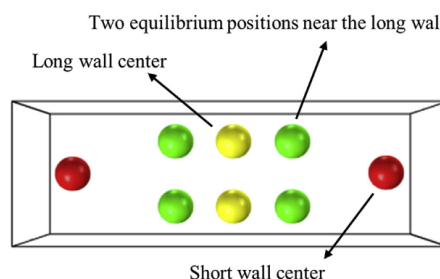


Figure 4: Different stabilized positions in a rectangular cross-section. Reprinted from (Mashhadian and Shamloo, 2019) with permissions.

3 MODEL AND COMPUTATIONAL SETUP

3.1 Numerical Model

We use well-established computational model of fluid and the immersed particles or cells. Here, the liquid is calculated with the lattice-Boltzmann (LB) method (Arnold et al., 2013). The cells are taken into account as immersed objects with fully 3D discretization using tetrahedrons that cover whole inner space inside the sphere. At the edges of the small tetrahedrons, fairly rigid springs are set so that the object almost does not undergo any deformation during the flow. Detailed description of the underlying models are available in (Jančigová et al., 2020; Jancigova and Tothova, 2014; Bachratý et al., 2018). The validation and verification of the computational models has been provided in (Jančigová et al., 2020; Jančigová, 2020; Tothova et al., 2015). For all simulations we used tetrahedral meshes with edges of sizes approximately $0.4 \mu m$.

3.2 Channel Geometry

Our aim is to simulate rectangular serpentine channels as depicted in Figure 2 (c₁). In the figure, there are only six S-shaped repeating sections displayed, however in practise, there are more sections needed to obtain desired focusing positions. Together with long straight channels before and after serpentine, the whole channel is too large to model at whole. Therefore we will model only one repeating section

(between the dashed seeding and reseeding line in Figure 5) enlarged by fluid evolution sections before and after, with periodical boundary conditions at the inflow and outflow. This way we ensure that the fluid is fully evolved at the seeding and reseeding lines. Periodicity of the middle section allows to reseed the cells back to the seeding line as soon as they reach the reseeding line. Their relative position at the cross section is preserved during the reseeding, as well as their velocity.

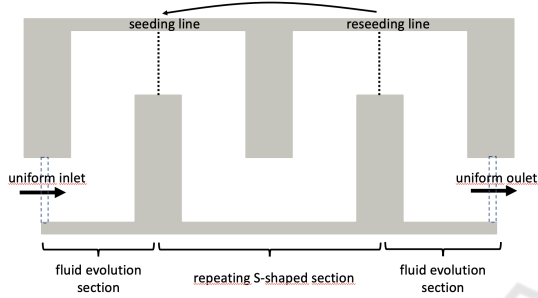


Figure 5: Simulation box for the case of the cross section with dimensions $80 \times 40 \mu\text{m}$. One repeating S-shaped sections enlarged by two fluid evolution sections.

After initial seeding of particles on the seeding line in the channel at the beginning of the flow, we watched the positions of the origins of the particles during the flow. When the particles have arrived to the reseeding line, we reseeded them back to the seeding line with the new coordinates of the particle origins and we have continued the watching of these origins coordinates. With this kind of reseeding by repeating the S-shaped section, as you can see on the picture in Figure 5, we have done a simulation of periodical flow without real construction of the real microchannel. As a result we get the trajectories (from the origin coordinates during the flow process). In Section 4 you can see analyses.

Since we study three different cross sections, the respective dimensions of the channels are different for all three cases. The respective dimensions of channels are depicted in Figure 6. Note that the lengths of the channel along the axial center of the channel are preserved.

3.3 Geometry and Fluid Set-up

To create a specific geometry as a serpentine channel, we need to define boundaries in the simulation box. This is done using geometrical shapes of rhomboids in the open-source scientific simulation package ESPResSo with PyOIF module (Jančígová et al., 2020).

To let the static fluid at the beginning of the simu-

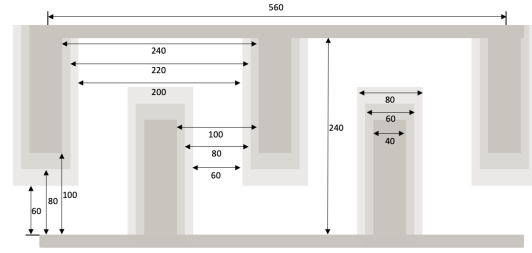


Figure 6: Dimensions of three different geometries in μm . The darkest boundaries represent $100 \times 32 \mu\text{m}$, the medium dark represent $80 \times 40 \mu\text{m}$ and the brightest represent $60 \times 52 \mu\text{m}$ cross section.

lation fully evolve, we simulate $500 \mu\text{s}$ without the particles. The uniform boundary conditions at inlet and outlet define the average velocity in the channel which is proportional to the volumetric flow rate. This can be done in PyOIF using a special velocity boundary (visualized in Figure 5 by dashed rectangles), with predefined constant values of velocity field at the boundary points.

Specific values of the inlet conditions and the corresponding flow rates are presented in Table 1.

Table 1: Fluid parameters in $80 \times 40 \mu\text{m}$ rectangular channel. Values in channels with other cross sections are similar.

Average velocity [$\mu\text{m}/\mu\text{s}$]	Reynolds number [-]	Volumetric flow [mL/min]
0.18	19.2	0.035
0.35	37.3	0.062
0.45	48	0.086
0.6	64	0.115

We are interested in studying the flows in physically relevant cases. We consider fluid with density and viscosity similar to physiological solutions or water being $1000 \text{kg}/\text{m}^3$ and $10^{-3} \text{Pa}\cdot\text{s}$. In inertial microfluidics, the relevant ranges for the Reynolds number are up to 100 (Ying and Lina, 2020). We consider four different average velocities up to $0.6 \text{m}/\text{s}$ in the channel so that Reynolds number varies up to 64. For maximal velocity for evaluation of Reynolds number in (5) we take the double of the average velocity. With cross sectional area of around $3100 \mu\text{m}^2$ it accounts for the volumetric flow rate being up to $0.115 \text{mL}/\text{min}$.

3.4 Particle Seeding

Since in various straight channels with a rectangular cross-section the particles in the flow settle in two stable positions over time, we also placed the particles in the running flow of the simulation in close neighbourhood of two concrete positions. We wanted the place-

ment randomly, so we used the normal distribution for seeding particles around this two positions. As you can see in Figure 7, we have three different geometries with particles seeded at the beginning of every simulation by normal distribution with same standard deviation, which we chose around the two positions.

In order to assure the reproducibility of the experiments we used the same random seeding for $5\mu\text{m}$ particles and $10\mu\text{m}$ particles.

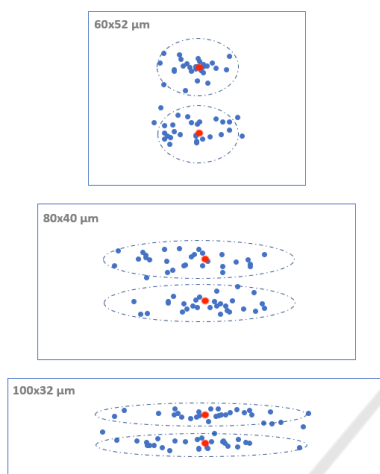


Figure 7: Three different cross sections of rectangular channels with particle seeding. Centers of the particles (blue dots) are depicted distributed by normal distribution around stable positions of straight channels (red dots).

4 COMPUTATIONAL RESULTS

Our aim is to examine how the stable positions within several cross-sections are dependent on geometric parameters of the channel. We compared three different cross-sections in square wave channel and in each cross section, we modified average fluid velocity and the size of the particles. The other parameters were kept constant. In Table 2 we present values of the parameters that were examined. Together we run 24 simulations.

Table 2: Overview of three varying parameters: size, velocity and cross section. Simulations have been performed for all 24 combinations.

Particle size μm	Average velocity $\mu\text{m}/\mu\text{s}$	Cross section $\mu\text{m} \times \mu\text{m}$
5	0.18	60×52
10	0.35	80×40
	0.45	100×32
	0.6	

4.1 Focusing Length

First we need to determine the focusing length of the channel. We tracked the trajectories of the cells until the particles reach stable region. Each of the 24 simulations was run such that at least 28 passes of the particles through the repeating S-section occurred.

In Figure 8 we see four $100 \times 32\mu\text{m}$ cases: 5 and $10\mu\text{m}$ particles each for two different Reynolds numbers. Horizontal axis shows the number of passes through the repeating S-shaped section and vertical axis shows the particle position along the width of the channel ranging from 0 to $100\mu\text{m}$ in these cases. We can clearly see when the particles start stabilize and we can define the minimal focusing length. In the figure we show trajectories for only two values of Reynolds number, however, taking account of all four values we arrive at the focusing length for cross section $100 \times 32\mu\text{m}$ to be 19 passes. Analogous we deduce 15 passes and 18 passes to be focusing lengths for $60 \times 52\mu\text{m}$ and $80 \times 40\mu\text{m}$, respectively.

After determining the focusing length, we further work with positions of particles across the channel width at the moment of passing this focusing length.

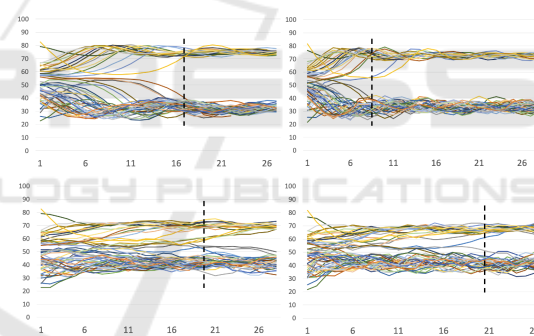


Figure 8: Trajectories of $5\mu\text{m}$ particles (top figures) and $10\mu\text{m}$ particles (bottom figures) in channel with $100 \times 32\mu\text{m}$ cross section for Reynolds number 37.3 (figures on the left) and 64 (figures on the right). Black vertical lines indicate minimal focusing length. Horizontal axis gives number of passes through the repeating S-section. Vertical axis gives particle position across the width of the channel.

4.2 Particle Separation

The three different geometries achieve different focusing performance for small and large particles. All three geometries have different focusing length but this is not a limitation: Once we pick the desired geometry, the channel length will be adapted accordingly. The particle focusing positions are either distinct and separated to more positions or focused along the center of the channel width. In some cases we could separate them, but in some cases they are fully

overlapping. The results are depicted in Figures 9 – 11.

For the case of 60×52 rectangular channel we assigned the smallest focusing length. The particles were focused already after 15 times of S-shaped sections repeating. However we get almost fully overlapping distributions of $5\mu\text{m}$ and $10\mu\text{m}$ particles across the channel width.

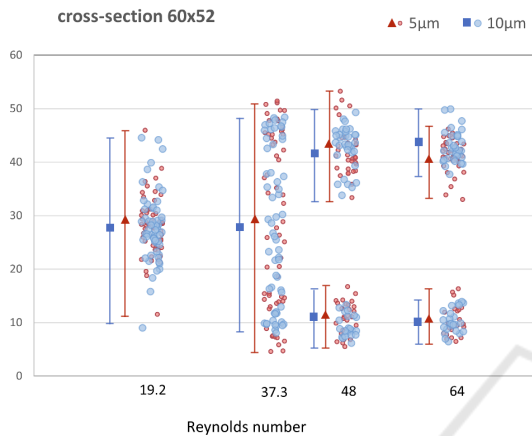


Figure 9: Particle focusing in $60 \times 52\mu\text{m}$ cross section for various Reynolds numbers. Focusing length was 15 passes of the repeating S-section. Vertical axis gives particle position in $[\mu\text{m}]$ across the width of the channel.

In 80×40 rectangular channel we can stop the simulations after 18 passes of S-shaped section. We can observe the best focusing performance for the Reynolds number between 32 and 50. The $5\mu\text{m}$ particles are separated in two positions across the channel width. The $10\mu\text{m}$ particles are focused along the center of the channel width, and the width of particle distribution gradually decreases to a single stable focusing line with higher Reynolds number. At Reynolds numbers 37.3 and 48 we can see in Figure 10 slightly overlapping of focusing sections for $5\mu\text{m}$ and $10\mu\text{m}$ particles which may result in non-perfect separation. This contributes to the best possibility of separating particles of two sizes. For the highest Reynolds number we can see overlapping of these two different particle sizes and it is not able to separate them.

For the case of 100×32 rectangular channel we needed 19 passes of the S-shaped section to get the best focusing of the particles. The $5\mu\text{m}$ particles have the best particle separation possibility. The focusing positions are fully distinct and we get the biggest gap between them as you can see in Figure 11, more than $30\mu\text{m}$ with Reynolds numbers 37,3 and 48. In this case, we have larger range of Reynolds numbers for separation.

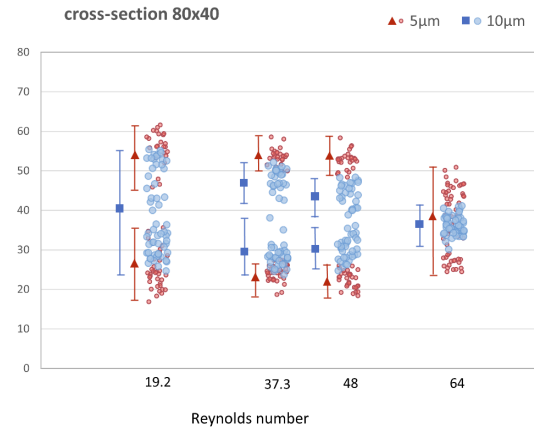


Figure 10: Particle focusing in $80 \times 40\mu\text{m}$ cross section for various Reynolds numbers. Focusing length was 18 passes of the repeating S-section. Vertical axis gives particle position in $[\mu\text{m}]$ across the width of the channel.

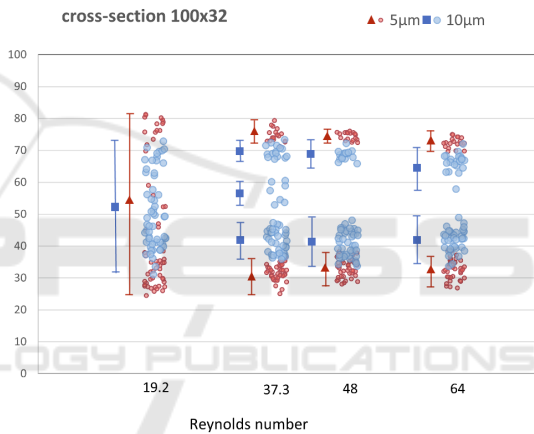


Figure 11: Particle focusing in $100 \times 32\mu\text{m}$ cross section for various Reynolds number. Focusing length was 19 passes of the repeating S-section. Vertical axis gives particle position in $[\mu\text{m}]$ across the width of the channel.

5 DISCUSSION

First of all we have very good agreement with results presented in (Ying and Lina, 2020) for the cross section $80 \times 40\mu\text{m}$. This validates our computational approach.

To compare various cross sections, we can draw several conclusions.

First observation is that the $60 \times 52\mu\text{m}$ cross section is not suitable for particle separation. Although the particles focused after the shortest distance, the focused position of particles overlap for both analyzed sizes.

As previous results from (Ying and Lina, 2020) suggested, a good candidate for separation is the

channel with $80 \times 40 \mu\text{m}$ cross section. This was confirmed by our computations and indeed, with Reynolds numbers 37 and 48 we get the possibility for particle separation. In this cross section, with higher Reynolds numbers we lose the possibility for separation because particles of both sizes drift towards the center of the channel. $10 \mu\text{m}$ particles focus in narrower strip (width $10 \mu\text{m}$) while $5 \mu\text{m}$ particles focus in wider strip (width $30 \mu\text{m}$). However, the two strips completely overlap.

The results for cross section $100 \times 32 \mu\text{m}$ give larger possibility for separation. Not only the offer separation for Reynolds numbers 37 and 48 but also at 64 we still have distinctive focusing position for particles of different sizes. Again, with increasing flow velocity we see tendency of particles to focus closer to the channel center, however this tendency is much weaker than for $80 \times 40 \mu\text{m}$ cross section and the particles still leave a particle-free strip in the middle of the channel. This results have two important consequences:

- Higher throughput is possible due to large Reynolds number and thus larger fluid velocity.
- Separation of even large particles is possible. Since $5 \mu\text{m}$ and $10 \mu\text{m}$ particles leave a particle-free strip in the middle of the channel, it may be possible to separate a third size of particles that would focus right in that strip.

This paper is expected to be instructive for optimization of inertial microchannel structures and for next bio-related studies and applications, for example blood cell separation in medicine.

ACKNOWLEDGEMENTS

This publication has been produced with the support of the Integrated Infrastructure Operational Program for the project: Systemic Public Research Infrastructure - Biobank for Cancer and Rare diseases, ITMS: 313011AFG5, co-financed by the European Regional Development Fund.

REFERENCES

Arnold, A., Lenz, O., Kesselheim, S., Weeber, R., Fahrenberger, F., Roehm, D., Košovan, P., and Holm, C. (2013). ESPResSo 3.1: Molecular dynamics software for coarse-grained models. In *Meshfree Methods for Partial Differential Equations VI*, Lecture notes in computational science and engineering, pages 1–23. Springer Berlin Heidelberg, Berlin, Heidelberg.

Bachratý, H., Bachratá, K., Chovanec, M., Kajánek, F., Smiešková, M., and Slavík, M. (2018). Simulation of blood flow in microfluidic devices for analysing of video from real experiments. In *Bioinformatics and Biomedical Engineering*, Lecture notes in computer science, pages 279–289. Springer International Publishing, Cham.

Cetin, B. and Li, D. (2011). Dielectrophoresis in microfluidics technology. *Electrophoresis*, 32(18):2410–2427.

Chun, B. and Ladd, A. J. C. (2006). Inertial migration of neutrally buoyant particles in a square duct: An investigation of multiple equilibrium positions. *Phys. Fluids (1994)*, 18(3):031704.

Di Carlo, D., Edd, J. F., Humphry, K. J., Stone, H. A., and Toner, M. (2009). Particle segregation and dynamics in confined flows. *Phys. Rev. Lett.*, 102(9):094503.

Forbes, T. P. and Forry, S. P. (2012). Microfluidic magnetophoretic separations of immunomagnetically labeled rare mammalian cells. *Lab Chip*, 12(8):1471–1479.

Gossett, D. R., Tse, H. T. K., Lee, S. A., Ying, Y., Lindgren, A. G., Yang, O. O., Rao, J., Clark, A. T., and Di Carlo, D. (2012). Hydrodynamic stretching of single cells for large population mechanical phenotyping. *Proc. Natl. Acad. Sci. U. S. A.*, 109(20):7630–7635.

Hood, K., Lee, S., and Roper, M. (2015). Inertial migration of a rigid sphere in three-dimensional poiseuille flow. *J. Fluid Mech.*, 765:452–479.

Jančigová, I. (2020). Computational modeling of blood flow with rare cell in a microbifurcation. In *Lecture Notes in Computational Vision and Biomechanics*, Lecture notes in computational vision and biomechanics, pages 518–525. Springer International Publishing, Cham.

Jančigová, I., Kovalčíková, K., Bohiniková, A., and Cimrák, I. (2020). Spring-network model of red blood cell: From membrane mechanics to validation. *Int. J. Numer. Methods Fluids*, 92(10):1368–1393.

Jancigova, I. and Tothova, R. (2014). Scalability of forces in mesh-based models of elastic objects. In *2014 ELEKTRO*. IEEE.

Jančigová, I., Kovalčíková, K., Weeber, R., and Cimrák, I. (2020). Pyoif: Computational tool for modelling of multi-cell flows in complex geometries. *PLoS Computational Biology*, 16:e1008249.

Jiang, D., Tang, W., Xiang, N., and Ni, Z. (2016). Numerical simulation of particle focusing in a symmetrical serpentine microchannel. *RSC Adv.*, 6(62):57647–57657.

Li, S., Ding, X., Guo, F., Chen, Y., Lapsley, M. I., Lin, S.-C. S., Wang, L., McCoy, J. P., Cameron, C. E., and Huang, T. J. (2013). An on-chip, multichannel droplet sorter using standing surface acoustic waves. *Anal. Chem.*, 85(11):5468–5474.

Martel, J. M. and Toner, M. (2014). Inertial focusing in microfluidics. *Annu. Rev. Biomed. Eng.*, 16(1):371–396.

Mashhadian, A. and Shamloo, A. (2019). Inertial microfluidics: A method for fast prediction of focusing pattern

- of particles in the cross section of the channel. *Anal. Chim. Acta*, 1083:137–149.
- Matas, J.-P., Morris, J. F., and Guazzelli, É. (2009). Lateral force on a rigid sphere in large-inertia laminar pipe flow. *J. Fluid Mech.*, 621:59–67.
- McLaughlin, J. B. (1993). The lift on a small sphere in wall-bounded linear shear flows. *J. Fluid Mech.*, 246(1):249–265.
- Ookawara, S., Higashi, R., Street, D., and Ogawa, K. (2004). Feasibility study on concentration of slurry and classification of contained particles by microchannel. *Chem. Eng. J.*, 101(1-3):171–178.
- Rasooli, R. and Çetin, B. (2018). Assessment of lagrangian modeling of particle motion in a spiral microchannel for inertial microfluidics. *Micromachines (Basel)*, 9(9).
- Segré, G. and Silberberg, A. (1961). Radial particle displacements in poiseuille flow of suspensions. *Nature*, 189(4760):209–210.
- Tanaka, T., Ishikawa, T., Numayama-Tsuruta, K., Imai, Y., Ueno, H., Matsuki, N., and Yamaguchi, T. (2012). Separation of cancer cells from a red blood cell suspension using inertial force. *Lab Chip*, 12(21):4336–4343.
- Tothova, R., Jancigova, I., and Busik, M. (2015). Calibration of elastic coefficients for spring-network model of red blood cell. In *2015 International Conference on Information and Digital Technologies*. IEEE.
- Ying, Y. and Lina, Y. (2020). Inertial focusing and separation of particles in similar curved channels. *Scientific reports, natureresearch*, 391:123570.

